Matter

CellPress

Article

Plasmon manipulation by post-transition metal alloying

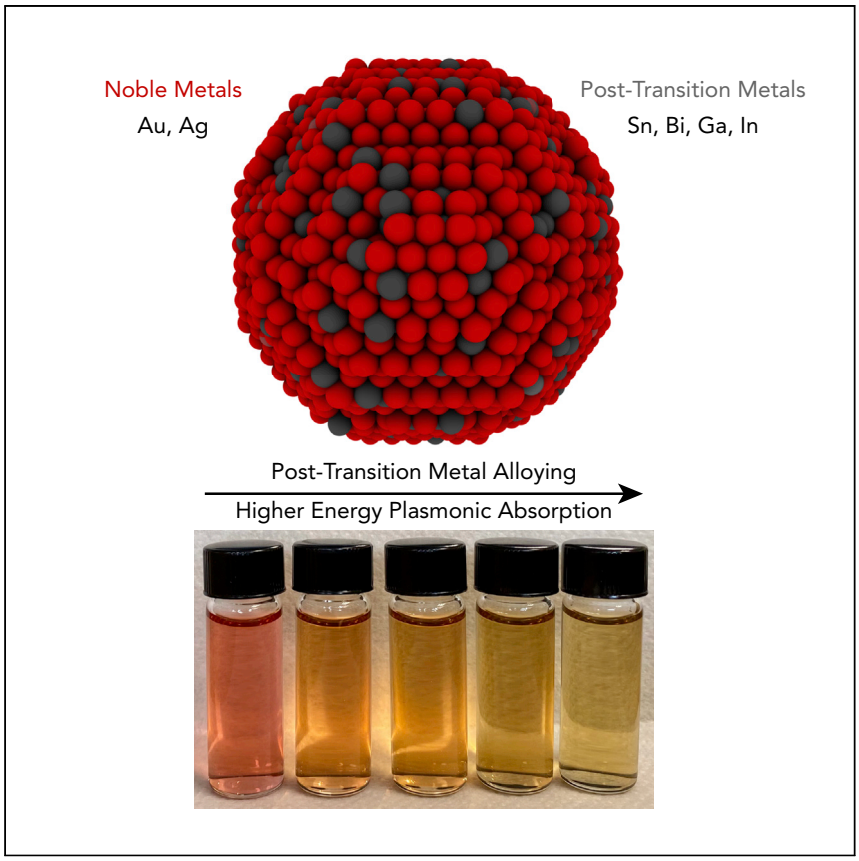

Noble metal nanoparticles efficiently absorb visible light and infrared light. Fonseca Guzman et al. show that, by alloying post-transition metals (e.g., Sn) into Au and Ag, plasmonic resonances can be tunably shifted to higher energies in the blue and UV that the individual noble metals cannot absorb. These multimetallic nanoparticles maintain efficient light absorption and contain a mixture of solid-solution alloys and intermetallic phases. Theoretical modeling further supports this as a general strategy for controlling light absorption in plasmonic multimetallic nanoparticles.

Maria V. Fonseca Guzman, Melissa E. King, Noah L. Mason, Connor S. Sullivan, Sangmin Jeong, Michael B. Ross

michael_ross@uml.edu

Highlights

Tunable plasmonic resonances achieved by alloying post-transition and noble metals

Efficient absorption with coexistence of substitutional alloys and intermetallics

Au and Ag LSPRs shifted into the blue and UV, respectively

Analytic and numerical modeling suggests generalizable strategy for plasmonics

Benchmark
First qualification/assessment of material properties and/or performance

Fonseca Guzman et al., Matter 6, 838–854
March 1, 2023
https://doi.org/10.1016/j.matt.2023.01.004

CellPress

Matter

Article

Plasmon manipulation by post-transition metal alloying

Maria V. Fonseca Guzman,[1] Melissa E. King,[1] Noah L. Mason,[1] Connor S. Sullivan,[1] Sangmin Jeong,[1] and Michael B. Ross[1,2,*]

SUMMARY

The design of new plasmonic materials is essential for continued progress in light manipulation at nanometer length scales. Often, multimetallic nanoparticles exhibit superior catalytic, mechanical, or corrosion-resistant behavior compared with their unary counterparts. Despite these advantages, designing multimetallic plasmonic materials remains challenging because, except for Au, Ag, and Al, most metallic elements exhibit poor plasmonic behavior. Here, we describe a strategy for manipulating the plasmon resonances of noble metal nanoparticles by post-transition metal alloying. We show how the metallic properties of post-transition metals—Bi, Ga, In, and Sn—can be imparted onto noble metals, enabling tunable higher-energy plasmon resonances that maintain high extinction coefficients and enter the UV. Theoretical modeling of simulated metallic mixtures and idealized Drude free-electron materials shows how this tunability is generalizable. Consequently, post-transition metal alloying provides a powerful strategy for realizing a new chemically diverse class of tunable plasmonic materials.

INTRODUCTION

Plasmonic metal nanoparticles absorb light with remarkable efficiency, enhance catalytic reactions through multiple mechanisms, and confine light into sub-nanometer volumes.[1–5] In many instances, however, they are limited by the few metals that support plasmon resonances. While multimetallic nanoparticles are ubiquitous in heterogeneous catalysis, solder, and structural materials, there are relatively few demonstrations of tunable and homogeneous multimetallic plasmonic materials.[6,7] Most hybrid multimetallic plasmonic materials are phase and function segregated,[3,6–8] while most homogeneously alloyed materials are limited in tunability or exhibit highly damped localized surface plasmon resonances (LSPRs).[9–13] All successful alloy demonstrations, such as Ag-Au, Al-Au-Ag, and Cu-Al, are limited in synthetic accessibility, spectral range, or oxidative stability.[6,12,14,15] Therefore, material strategies that can directly and deliberately control the metallic properties that dictate the LSPR are needed to realize new classes of functional plasmonic materials.

RESULTS

Designing post-transition-metal-noble-metal plasmonic alloys

Post-transition metals (PTMs) provide an intriguing class of elements to combine with the plasmonically conventional noble metals (NMs). In contrast with most transition metals, PTMs have Drude-like metallic properties that enable UV LSPRs by virtue of their high carrier densities and high energy plasma frequencies (Figures 1 and S1).[12,16–18] Unlike most transition metals, PTMs exhibit covalency originating from

PROGRESS AND POTENTIAL

Light-absorbing materials are critical for advances in energy, medicine, and information transfer. While metal nanoparticles absorb light more efficiently than most forms of matter, they are limited in the wavelengths they can absorb as well as in their composition. This reduces opportunities for these so-called plasmonic nanoparticles to impact new technologies.

Here, we control where plasmonic nanoparticles absorb light by creating metallic mixtures. By diffusing unconventional plasmonic metals, such as tin, into traditional ones, such as silver or gold, we create metallic mixtures that strongly absorb blue and UV light that the traditional metals cannot absorb. These materials show immense complexity in how the atoms are arranged with remarkable tunability, motivating exploration of an almost limitless number of metallic combinations. We envision that these materials could lead to a broader scope of opportunities for plasmonics with reduced noble metal usage.

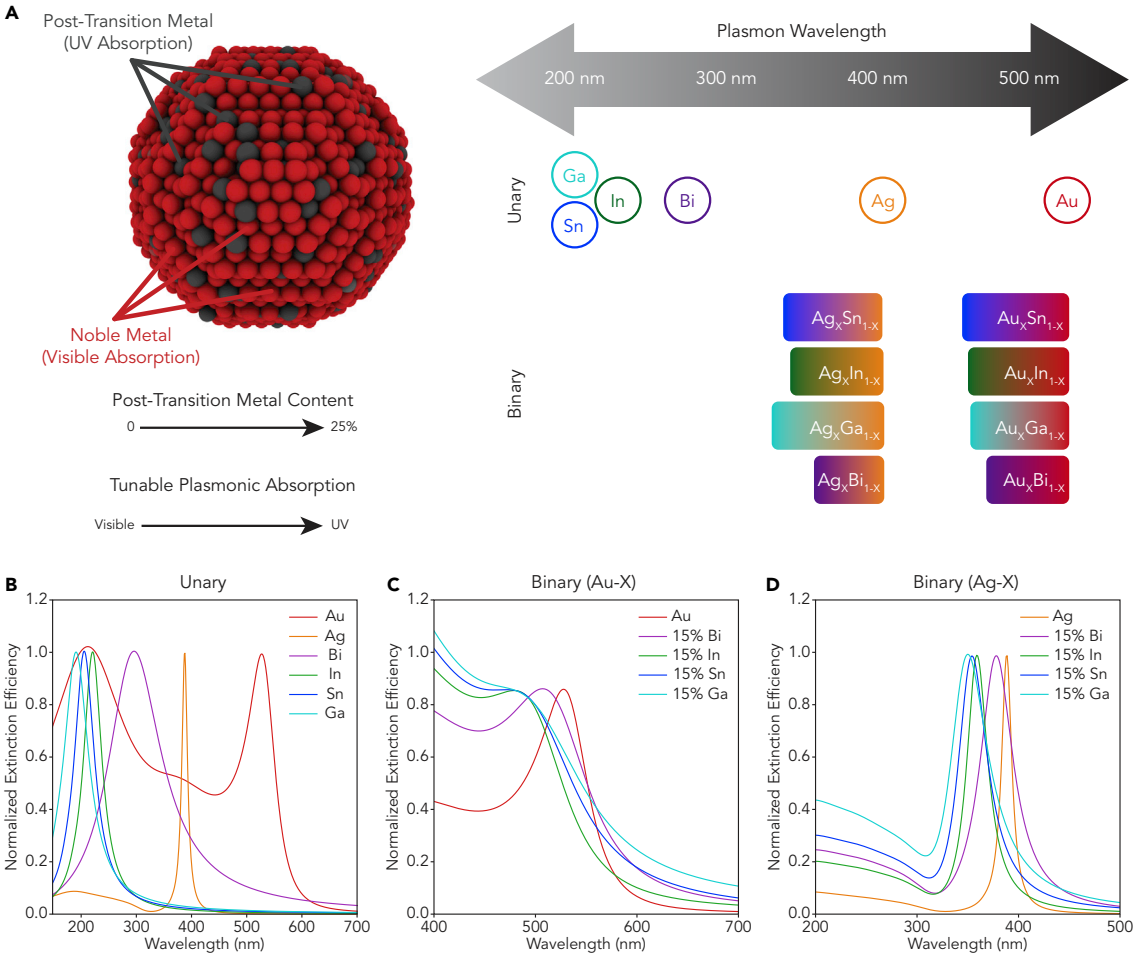

Figure 1. NM plasmon manipulation by PTM alloying

(A) PTM incorporation is predicted to shift NM LSPRs toward higher energy because of the intrinsic UV-resonant behavior of PTMs. This is realized experimentally with Au-Bi, -Ga, -In, and -Sn and Ag-Sn nanoparticles.

(B) Mie theory calculated extinction spectra for unary 20-nm-diameter spheres.

(C) Mie theory calculated extinction spectra for 20-nm spheres comprising 15% Bi-, Ga-, In-, and Sn-Au linearly weighted dielectric functions. See also Figures S2–S4.

(D) Mie theory calculated extinction spectra for 20-nm spheres comprising 15% Bi-, Ga-, In-, and Sn-Ag linearly weighted dielectric functions. See also Figure S5.

their *p*-block character; alloying with NMs could enable creation of plasmonic materials with distinct chemical, physical, and bonding characteristics.[19,20] Conceptually, alloying could systematically alter the metallic properties of the NMs, resulting in tunable higher-energy LSPRs as a function of composition (Figure 1A).

Classical Mie calculations using linear combinations of the NM and PTM dielectric functions were used to approximate the optical response of idealized PTM-NM solid solutions. While an approximation,[12] previous literature has shown that linearly weighted dielectric functions can simulate the Drude response and dispersion of the dielectric function.[21] Our recent work showed theoretically that many of the PTMs (excluding Bi) are Drude-like in their response, both by visual inspection of their dielectric functions and analysis of their plasmon line widths.[16] Generally, plasmonic metals are described using the free-electron Drude model in the long-wavelength region (away from interband transitions and above the plasma frequency). In

[1]Department of Chemistry, University of Massachusetts Lowell, Lowell, MA 01854, USA
[2]Lead contact
*Correspondence: michael_ross@uml.edu
https://doi.org/10.1016/j.matt.2023.01.004

other words, we assume (and see experimentally) that the plasmonic response is dominated by the free electron properties of a metal.[21]

Deviations can be expected from this simple theory at high (>25% mixing) metal ratios for intermetallics where ordered unit cells give rise to distinct band structures and due to the emergence of interband transitions that are distinct from those in the constituent metals (Note S1).[6,11,12,21,22] Qualitative analysis of the mixed dielectric functions shows that increasing the PTM content makes the real part of the dielectric function more negative, enabling higher-energy LSPRs, while increasing the lossy imaginary part (Figures S2 and S3).

The unary PTMs (Bi, Ga, In, and Sn) exhibit sharp plasmon resonances in the UV ranging from ~200–300 nm, while the NMs exhibit characteristic LSPRs at 395 nm for Ag and 520 nm for Au (Figure 1B). In contrast, the binary PTM-NM LSPRs are shifted to higher energy. At 15% PTM content, the LSPRs for Au-X materials are shifted to ~460 nm, while the LSPRs for Ag-X materials blueshift to ~340 nm for 15% Ag_xGa_{1-x} (Figures 1C, 1D, S4, and S5). For all PTM-NM combinations, varying the amount of PTM enables tuning of the LSPR over a wide range (~0.5 eV; Figure S6). Given this qualitative theoretical evidence for PTM-mediated plasmonic manipulation, we sought to realize these materials experimentally.

Tunable plasmonic Au-Sn alloys and intermetallics

Au-Sn was selected as a model system because of the well-known synthetic and plasmonic behavior of Au, the well-studied phase behavior of bulk Au-Sn, and the UV plasmonic activity of Sn (Figure 2A).[16,23] PTM-NM nanoparticles were synthesized using a seeded chemical reduction of Sn^{4+} (experimental procedures). Aqueous ~15-nm citrate-capped Au nanoparticles were used as seeds because of their colloidal stability, compatibility with the $SnCl_4$ precursor, and labile nature of the citrate capping agent (Figure 2B). Incorporation of Sn was controlled by modifying the added Sn amount, while inductively coupled plasma-mass spectrometry (ICP-MS) and energy-dispersive X-ray spectroscopy (EDS) were used to quantify the percentage of Sn incorporation (Table S1). This approach was found to yield uniform, spherical, and monodisperse (<15% coefficient of variation) nanoparticles for all compositions investigated (Table S2; Figures S7 and S8).

Blue-shifting of the LSPR is observed upon incorporation of Sn into the Au seeds (Figure 2E). Specifically, UV-visible extinction spectroscopy reveals a sharp feature at 520 nm (Au seeds) that shifts to 507, 497, and 477 nm for 8%, 20%, and 25% Sn incorporated amounts, respectively (Figure S9; Table S3). At low Sn content, the LSPR retains much of the Au-character, while increasing the Sn content broadens the resonance. These changes in optical extinction are visually apparent, changing the appearance from burgundy for the Au seeds through a series of orange, yellow, and brown shades with increasing Sn content (Figure 2D). Transmission electron microscopy (TEM) reveals that the nanoparticles remain spherical and uniform after Sn incorporation (Figures 2C, S7, and S8), and long-term characterization reveals that the optical response of the nanoparticles is relatively stable for at least 2 weeks (Figure S10).

High-angle annular dark-field scanning TEM (HAADF-STEM) coupled with EDS was used to better understand the structure of the multimetallic nanoparticles (Figures 2F–2U and S11). Elemental mapping shows that the Sn diffuses through the volume of the nanoparticle, though it appears visually to be richer in proportion at the periphery.[24,25] Similar syntheses caused intermetallic nucleation at the core,

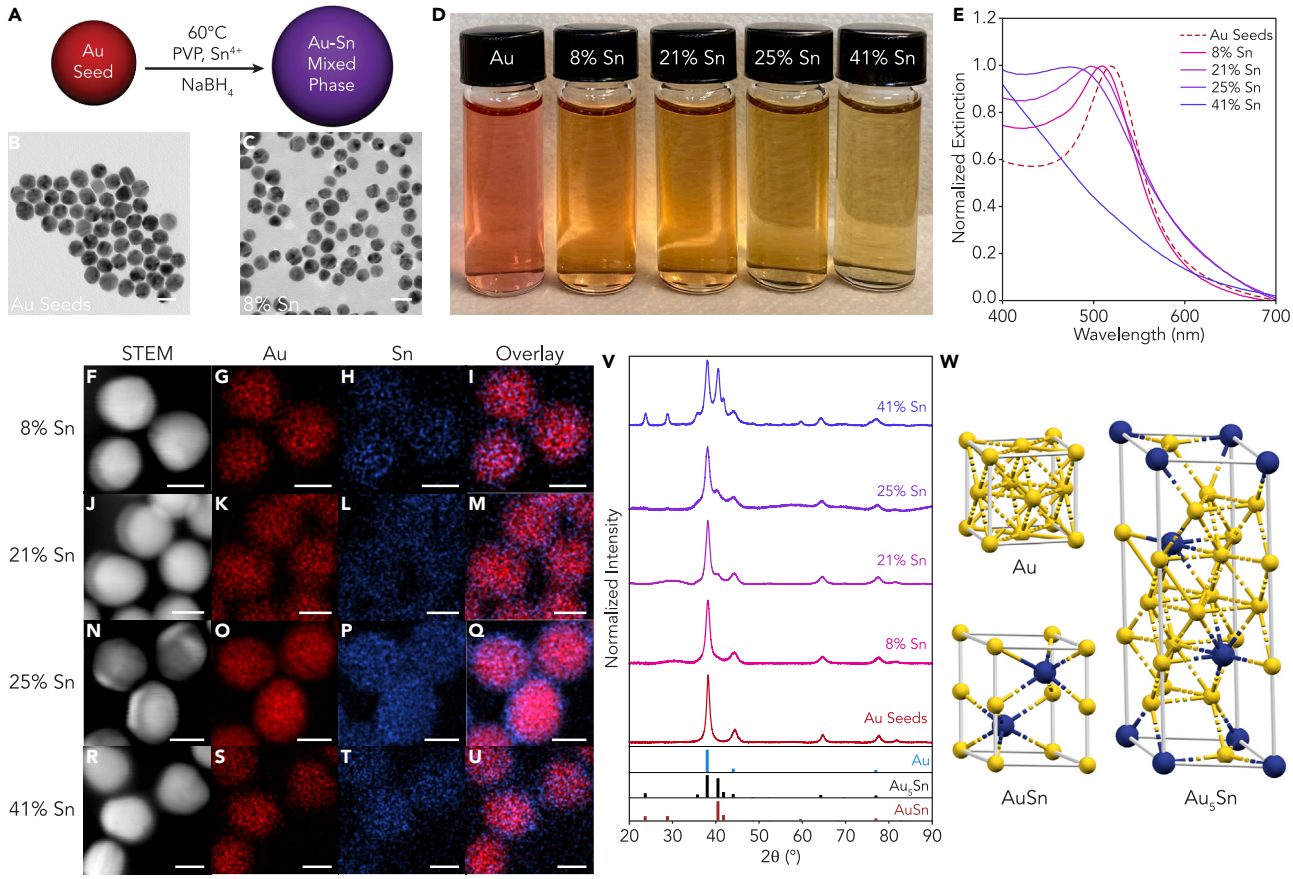

Figure 2. Binary Au-Sn plasmonic alloy nanoparticles

(A) Schematic of the seeded method for synthesizing Au-Sn nanoparticles.

(B and C) Transmission electron micrographs of (B) Au seeds and (C) 8% incorporated Sn nanoparticles. Scale bars, 20 nm. See also Figure S7 and Table S2.

(D) Photograph of the colloidal solutions of Au seeds and the 8%, 21%, 25%, and 41% Sn composition nanoparticles.

(E) Normalized extinction spectra for Au seeds and 8%, 21%, 25%, and 41% Sn nanoparticle compositions.

(F–U) HAADF micrographs (F, J, N, R) and STEM-EDS maps of Au (G, K, O, S), Sn (H, L, P, T), and the Au-Sn overlay (I, M, Q, U) for the 8%, 21%, 25%, and 41% Sn composition nanoparticles. Scale bars, 10 nm. See also Figures S11 and S12.

(V) Powder XRD patterns for the Au seeds and the 8%, 21%, 25%, and 41% composition nanoparticles. Reference stick patterns for Au, AuSn, and Au_5Sn are included at the bottom. See also Figures S13–S15.

(W) Representations of the relevant unit cells.

amorphous Au-Sn shells, or the presence of Au-rich solid-solutions.[24–26] These studies also suggest that Au diffusion through Sn occurs more rapidly than the inverse, although both are possible, and interdiffusion can be observed in nanoscale systems.[25] The bulk phase diagram as well as previous literature suggest that many of these phases can co-exist.[23–28] However, neither the images nor mapping suggest the presence of well-separated core-shell structures. EDS line scans through the nanoparticle show Sn distributed throughout, while mapping suggests an Sn-rich outer region (Figure S12). Thus, the structure appears to be Sn rich at the periphery, with Sn incorporated throughout the interior volume.

X-ray diffraction (XRD) and X-ray photoelectron spectroscopy (XPS) were used to better understand the atomic and structural phase behavior (Figure 2V). At low (8%) Sn content, broadening and shifting of the Au (111) peak is observed, indicative of substitutional alloying (Figure S13; Note S2). With increasing Sn content, the trigonal Au_5Sn

Table 1. Extinction coefficients for Au-Sn mixed-phase plasmonic nanoparticles

Au: Sn Mole Ratio	LSPR (nm)	Radius (nm)	Extinction coefficient (M^{-1} cm^{-1})
Pure Au	523	15.0 ± 1.5	4.56 ± 0.03 × 10^8
12:1 (8% Sn)	507	16.8 ± 1.5	1.33 ± 0.02 × 10^9
4:1 (21% Sn)	497	17.8 ± 1.3	8.94 ± 0.05 × 10^8
3:1 (25% Sn)	477	18.0 ± 1.4	6.94 ± 0.04 × 10^8

See also Figure S21 and Table S5.

phase (up to 21% Sn) and then the hexagonal AuSn phase (25% and 41% Sn) are observed (Figure 2W). However, a Au-like face-centered cubic (fcc) pattern is retained in all cases. Rietveld analysis suggests that increasing the Sn content leads to a monotonic increase in Au_5Sn formation for 8%, 21%, and 25% Sn incorporation (Figures S14 and S15). Because the Au fcc pattern is retained with consistent Vegard's-like shifting of the (111) peak, the intermetallic phases likely co-exist with a substitutional Au_xSn_{1-x} alloy phase; a variety of eutectic mixtures has been observed previously in Au-Sn.[24–28] To account for the measured Sn content (8%, 21%, and 25%), some extent of substitutional mixing in the Au-phase is likely, given that the intermetallic phases are not sufficiently Sn rich (12.5% in Au_5Sn, 50% in AuSn). XPS further supports this analysis; the measured surface content is greater than the measured Sn content in the full volume of the nanoparticle (Table S4; Figure S16), further supporting the existence of a Sn-rich periphery.

To probe the relation between optical and structural properties and better understand the diffusion of Sn into the Au seed, syntheses were conducted where the temperature and reducing agent amounts were systematically varied. Synthesis at 60°C was found to give the most blue-shifted LSPR and the greatest relative amount of Au_5Sn phase (Figure S17). By comparison, lower temperatures (40°C and room temperature) resulted in broadened LSPRs that were minimally blue-shifted; these temperatures also led to formation of greater fractions of AuSn. At 80°C minimal shifting is observed and the LSPR resembles that of the unreacted Au seeds. These data suggest that the most blue-shifted LSPRs occur when Au/Au_xSn_{1-x} and intermetallic (Au_5Sn + AuSn) content is present (Figures S18 and S19). These differences are likely due to competition between interdiffusion rates of Au and Sn as well as stabilization of thermally favored intermetallic phases. Varying the amount of reducing agent results in structures that either incorporate less Sn, as evidenced by less blue-shifted LSPRs and less intermetallic content, or irreversibly aggregate upon reduction (Figure S20).

Quantification and theoretical analysis of the plasmonic response

To quantify the impact of Sn incorporation on the plasmonic response, extinction coefficients for the plasmonic nanoparticles were quantified (experimental procedures). As anticipated, Table 1 shows that the extinction coefficients of the Au-Sn nanoparticles are within an order of magnitude of the Au seeds up to 25% Sn incorporation (Table S5; Figure S21). Therefore, Au-Sn nanoparticles support highly efficient LSPRs despite being composed of up to 25% PTM.

To better understand the relationship between metallic properties and optical response, theoretical Mie theory calculations were performed using real material dielectric functions and idealized Drude metals. Material dielectric functions enable direct comparison with experiments, while idealized Drude dielectrics functions enable formation of a generalized understanding of what properties influence the LSPR. Linear combinations of the Au and Sn dielectric functions (Figures 1, 3A, and S22) were found to give reasonable agreement with experiments, capturing the LSPR blue-shift and

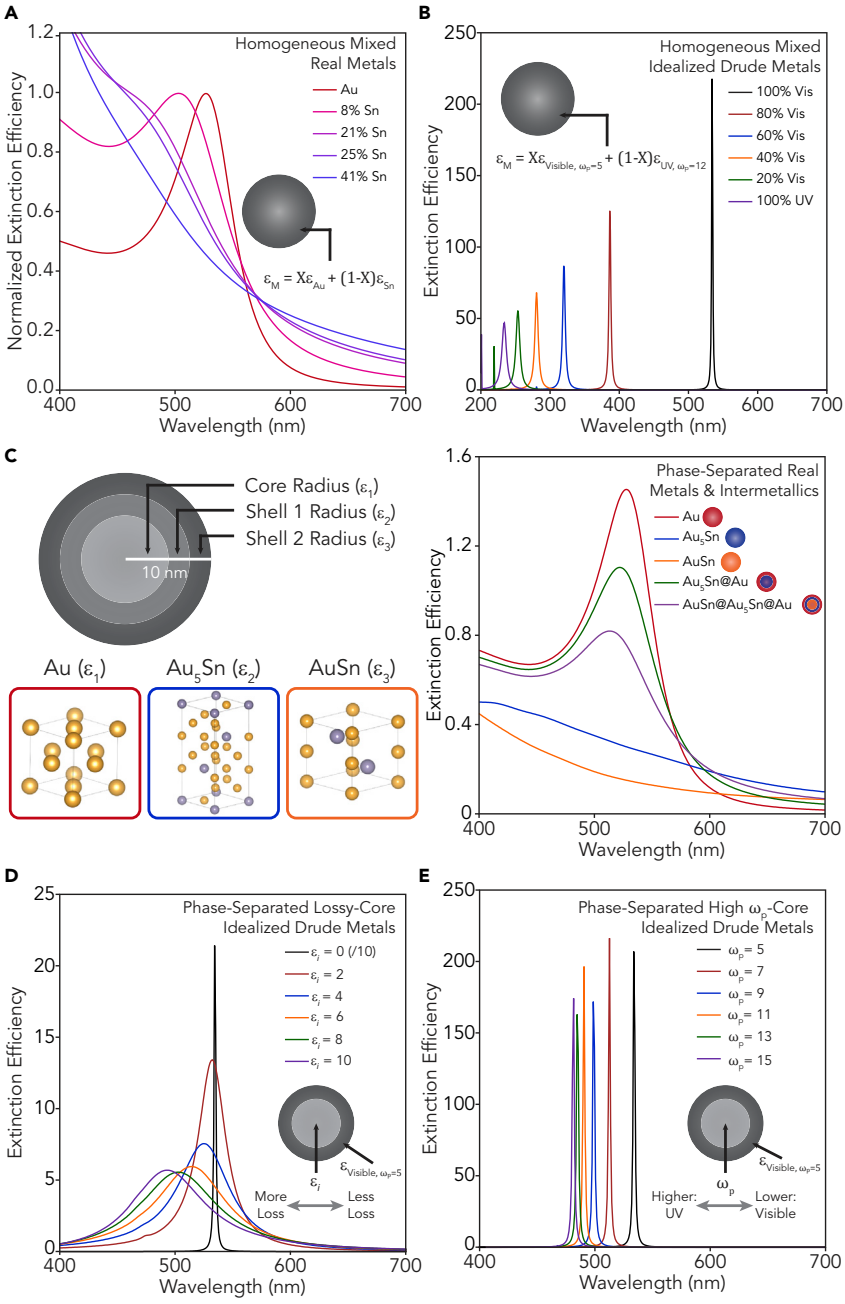

Figure 3. Optical modeling of the binary Au-Sn plasmonic response

(A) Mie theory modeling of linearly mixed dielectric functions for Au-Sn materials. 10-nm-radius spheres were simulated using Mie theory with 0% (Au), 8%, 21%, 25%, and 41% Sn linear mixtures as dielectric functions. See also Figure S22.

(B) Mie theory modeling of mixed dielectric functions for idealized visible (ω_p = 5, LSPR ~550 nm) and UV (ω_p = 12, LSPR ~225 nm) Drude materials. See also Figure S24.

(C) Schematic and Mie theory modeling of intermetallic and core-shell structures. Au (red), Au_5Sn (blue), and AuSn (orange) dielectric functions adapted from Leitao et al.[22] were used as input. In addition, Au_5Sn core @Au shell (5, 10 nm radius) and AuSn core-Au_5Sn shell-Au shell (3.33, 6.67, 10 nm radius) spheres are included for comparison. See also Figures S25 and S26.

Figure 3. *Continued*

(D) Mie theory modeling of core-shell structures with idealized Drude materials where the shell (10-nm radius) is a lossless visible (ω_p = 5) plasmonic material, and the core (5-nm radius) is the same visible plasmonic material with an increasingly lossy dielectric function. See also Figure S27.

(E) Mie theory modeling of core-shell structures with idealized Drude materials where the shell (10-nm radius) is a lossless visible (ω_p = 5) plasmonic material, and the core (5 nm radius) has an increasing plasma frequency. See also Figure S28.

broadening with increasing Sn content (Figures 2E and S23; Table S3). This is despite these models not being able to fully capture the changes in the metal band structure that occur because of alloying (Note S1). Linear combinations of UV (ω_p = 12, LSPR ~225 nm) and visible (ω_p = 5, LSPR ~550 nm) active idealized Drude materials were constructed to test the generality of this observation (Figure S24). Here, a blue-shifted and broadened LSPR was observed as the UV-active material content increased (Figure 3B). In this idealized Drude case, linear mixing approximates the properties of a substitutional alloy, given that these fictitious Drude materials do not have interband-driven loss (they are lossless by design).

To investigate the plasmonic response of the phase-separated mixed-phase materials, core-shell Mie simulations were performed using intermetallic dielectric functions (Figure 3C) that were calculated previously (Figure S25).[22] A series of pure-phase and core-shell segregated structures was chosen as a model system for phase-separated pure-phase intermetallic structures. The pure intermetallics do not support a strong plasmonic response, in agreement with previous observations (Figure 3C; Note S3).[22,29,30] The core-shell structures, however, do support robust LSPRs and approximate the experimental trend: a blueshift is seen when the intermetallic core is surrounded by a pure Au shell (Figure 3C). Notably, the inverse structure, the Au core intermetallic shell, shows no evidence of an LSPR (Figure S26). These data are thus consistent with the experimental observation of a Sn-rich outer region putatively comprising a substitutional alloy/intermetallic mixture rather than a distinct Au@intermetallic core-shell structure.

The idealized Drude model was further developed to describe a core-shell structure where the shell is a visible active plasmonic metal while the core comprises an increasingly lossy metal (Figures 3D and S27) or a metal with an increasingly high-energy LSPR (Figures 3E and S28). These dielectric functions with tunable loss approximate the intermetallic dielectric functions, which do not support LSPRs, while allowing one to independently investigate how the distinct metallic properties that change in alloys and intermetallics can together dictate the collective LSPR of mixed-phase nanoparticles. An increasingly lossy core (Figure 3D) and an increasingly high-energy plasmonic core (Figure 3E) were found to blue-shift the LSPR; however, only the increasingly lossy core results in significant broadening.[2,4,31]

The combined optical, structural, and theoretical data suggests that PTM alloying can manipulate the plasmonic response by two primary mechanisms: modification of the Drude response by formation of Sn-enriched Au substitutional alloys (Figures 3A and 3B) and by nucleation of phase-separated Au and Au-Sn intermetallic phases (Figures 3C–3E). These models are consistent with the experimental Au-Sn model system, where a Sn-rich region exists on the periphery of the nanoparticle, while Au_5Sn and AuSn intermetallic phases co-exist with Au/Au_xSn_{1-x} solid solutions. Both mechanisms can contribute to the observed plasmonic tunability, while the presence of the intermetallic is associated with some damping and

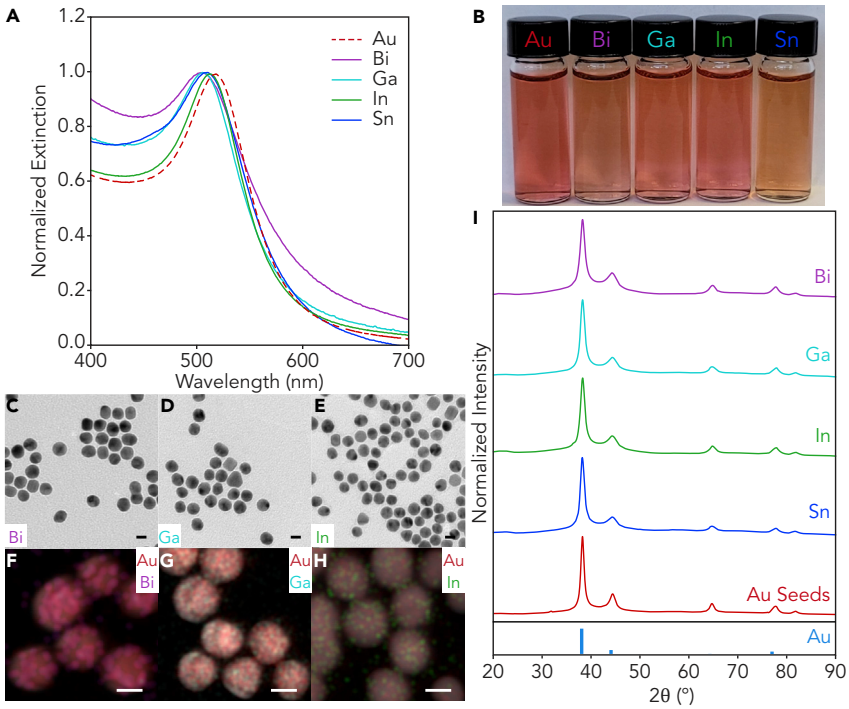

Figure 4. Plasmonic tunability with Bi, Ga, and In

(A) UV-visible spectra for Au seeds (red) and Au-Bi (purple), Au-Ga (cyan), Au-In (green), and Au-Sn (blue) nanoparticles.

(B) Photograph of the colloidal solutions of nanoparticles.

(C–H) TEM micrographs and STEM-EDS overlay maps for 10% added Bi (C, F), Ga (D, G), and In (E, H) nanoparticles. See also Figures S29 and S30 and Table S8.

(I) Powder XRD patterns for the Au seeds and the 10% molar equivalent added Bi, Ga and In, and Sn nanoparticles. A reference stick pattern for Au is included at the bottom. Scale bars, 10 nm. See also Figure S31.

broadening. Importantly, the idealized Drude models suggest that this approach to tuning NM LSPRs is generalizable.

Generalizing NM and PTM alloys for plasmonics

To demonstrate the general strategy of plasmon manipulation by PTM alloying, tunable LSPRs were achieved by alloying additional PTMs (Figure 4) as well as by using Ag as the NM base material (Figure 5). To incorporate Bi, Ga, and In, the synthesis described above was modified by varying the temperatures of the incubation and alloying steps and adding 10% molar equivalent PTM (experimental procedures). In all cases, incorporation of the PTM resulted in a visible color change (Figure 4B), and the LSPR was blue-shifted (Figure 4A) from the characteristic 520 nm LSPR for the Au spheres, with Au-Bi nanoparticles at 504 nm, Au-In at 512 nm, and Au-Ga at 505 nm. TEM micrographs (Figures 4C–4E) show that the alloyed nanoparticles are spherical and homogeneous in size (<10% coefficient of variation; Table S6), while STEM-EDS maps show that their composition is relatively uniform (Figures 4F–4H, S29), although line scans of the Au-Bi and Au-In structures suggest an outer PTM-rich region similar to that observed for the Au-Sn structures (Figure S30). We note, however, that detailed structural characterization is more challenging because post-synthetic oxidation occurs more rapidly for these systems compared with the Au-Sn systems, which exhibit approximately month-long stability (Figure S10).

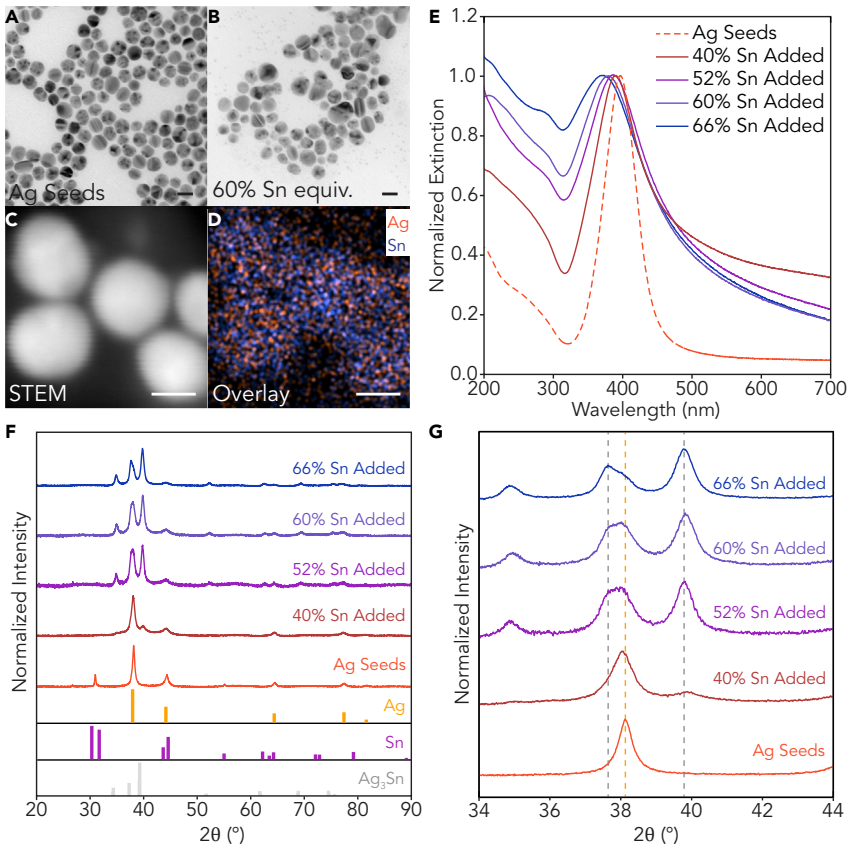

Figure 5. Binary Ag-Sn plasmonic alloy nanoparticles

(A and B) TEM micrographs of (A) Ag seeds and (B) 60% Sn added nanoparticles. See also Figure S34 and Table S9. Scale bars, 20 nm.

(C and D) HAADF micrographs (C) and STEM-EDS overlay maps (D) for 60% Sn added. Scale bars, 10 nm. See also Figures S36 and S37.

(E) UV-visible spectra for Ag, 40%, 52%, 60%, and 66% Sn molar equivalent added nanoparticles.

(F) Powder XRD patterns for Ag, 40%, 52%, 60%, and 66% Sn added nanoparticles.

(G) Inset: powder XRD pattern focusing near the Ag (111) peak. Reference stick patterns for Ag, Sn, and Ag_3Sn are included at the bottom.

See also Figures S41 and S42.

XRD of the PTM alloys shows a Au-like fcc pattern that is suggestive of substitutional alloying (Figure 4I), similar to what is observed for low-Sn-content alloys (Figure 2U), where no intermetallic phases were observed but subtle broadening and shifting of the (111) and (200) peaks occurs (Figure S31). ICP-MS was used to quantify the PTM content, and Bi was determined to be present at ~6% and In at ~9% (Table S7). Ga was only detectable in trace amounts; we note, however, that the Au-Ga nanoparticles were metastable in solution during the centrifugation and processing process necessary for rigorous characterization. XPS suggests that a surface-rich PTM region exists on the periphery, similar to that observed for the Au-Sn nanoparticles (Table S7; Figure S32), and the optical response cannot be explained by the presence of unreduced salt coordination or formation of oxide shells, both of which would red-shift the LSPR (Figure S33).[2,6]

Differences in the optical response and structural behavior between Au-PTM alloys are likely due to the different molar compositions achieved and differences in the intrinsic electronic properties of the PTMs (Figures S1–S3). Structural differences

are ascribed to differences in diffusion in the Au lattice, phase behavior, and oxidation potentials of the PTMs investigated. For example, oxidation of Au-In nanoparticles has been observed previously in aqueous alloy Au-In nanoparticles, resulting in formation of an Au core@In_2O_3 shell with a red-shifted LSPR.[32] These data suggest that the presence of an intermetallic phase in the Au-Sn systems confers colloidal stability in contrast to the non-intermetallic Au-PTM alloy nanoparticles. Overall, the blue-shifted LSPRs observed for the low-PTM-content NM alloys are qualitatively similar, likely because of their similarly dispersive real dielectric functions in the visible and UV (Figures S1–S3).

A seeded co-reduction approach (Figure 5; experimental procedures) was used to synthesize Ag-Sn alloy nanoparticles with a less than 20% coefficient of variation (Figures S34–S35; Table S9). TEM, HAADF-STEM, and EDS mapping and line scans show that the nanoparticles are relatively consistent in Sn content (Figures 5A–5D and S35–S37). ICP-MS (Table S10) and XPS (Figure S38; Table S11) suggest that a Sn-rich periphery is present, analogous to that seen in Au-Sn and other Au-PTM alloy nanoparticles. Optically (Figure 5E), Sn alloying blue-shifts the LSPR from the visible (~400 nm for the Ag seeds) to the UV (365 nm at 23% Sn content). With increasing Sn content, the LSPR line shape asymmetrically broadens toward the blue, possibly because of the formation of new interband transitions.[33] However, a clear Ag-LSPR-like extinction feature is maintained up to ~23% Sn incorporation. Mie simulations incorporating linearly weighted Ag and Sn dielectric functions qualitatively capture the blue-shifted LSPRs of the Ag-Sn combinations (Figures S39 and S40). Overall, the optical data show that an Ag-like LSPR is retained, while tunability toward higher energy can be achieved.

Like in the Au-Sn system, XRD reveals formation of an intermetallic phase (Ag_3Sn) with greater added Sn amounts (Figure 5F). Shifting and broadening of the fcc (111) peak is observed for the low-Sn-content nanoparticles (Figures 5F and 5G), indicative of substitutional alloying (Note S2). Interestingly, Ag_3Sn phase content is seen to increase with increased added Sn equivalents (Figures S41 and S42) despite the overall Sn content changing by only a few percent (Tables S10 and S11). It could be that additional Sn stabilizes intermetallic phases, as seen in the Au-Sn system, although the differences in optical response and Ag_3Sn phase content suggest that a more complex structural change is occurring. This observation, combined with the XPS surface content quantification and peak shifting in the XRD pattern, could suggest strain in part because of the outer Sn-rich region, although further structural investigation is needed.

DISCUSSION

In the two archetypal plasmonic materials, Ag and Au, PTM alloying is shown to enable tunable higher-energy plasmon resonances. This tunability is seen in the presence of NM-rich solid solutions as well as ordered intermetallic phases. This tunable ability to achieve higher-energy plasmonic resonances is in contrast with the well-known strategies of controlling plasmonic resonances by changing the nanoparticle size, shape, and environment, all of which red-shift plasmonic absorption toward lower energies. This observation presents new questions relating to our understanding of plasmonic resonances in mixed metallic systems, whereby phase-separated materials exhibit high quality LSPRs in a tunable manner. Advanced spectroscopic, structural, and electron microscopy characterization will be needed to reveal the underlying fundamental principles that dictate this behavior. The interplay between the formation of intermetallic phases and their spatial segregation is critical

for understanding the optical and structural differences observed between NM-PTM alloys. Additional theoretical work is needed to better simulate and understand the dielectric functions of alloys and intermetallics, ideally in such a way that novel plasmonic alloys can be designed using *ab initio* methods. While linear combinations of alloys approximate the behavior observed here, more rigorous methods are needed to fully understand the optical response. Finally, while we have shown that several putative mixed-phase alloy/intermetallic structures can give rise to this tunability, the mixed-phase nanoparticles investigated here are not exhaustive. We are only beginning to understand the role of phase and metallic mixing at the atomic scale and nanoscale in plasmonic materials and how these together can reveal new strategies for plasmonic control.

The ability to maintain high-quality plasmon resonance in materials with high intermetallic (>25%) and PTM (>25%) content enables future studies that leverage chemical and metallic properties beyond those accessible with NMs.[5,13,17] PTMs have properties distinct from transition metals, including covalent and directional bonding, complex phase diagrams, and catalytic activity.[19,20,34] Intermetallic and solid solutions are commonplace in heterogeneous catalysis because of their well-defined atomic arrangements and distinct properties compared with their unary constituents.[7,34–36] Finally, tuning plasmonic absorption is important for activating biomolecules and aligning resonances with photoredox catalysts and UV polymerizations.[34,36] When taken together, this work suggests that control over phase, crystal structure, and spatial distribution of nanoscale metals can have a profound and highly tunable influence on plasmonic absorption. The realization of robust plasmonic properties in NM-PTM nanostructures potentially enables future discovery and application of multimetallic plasmonic nanoparticles for sensing, catalysis, phase-change materials, hybrid absorbers, and optoelectronic materials.

EXPERIMENTAL PROCEDURES

Resource availability

Lead contact

Further information and requests for resources should be directed to the lead contact, Michael B. Ross (michael_ross@uml.edu).

Materials availability

The materials used here can be synthesized according to the procedures included using commercially available reagents. Detailed methods can be found in the supplemental information.

Data and code availability

All experimental and theoretical data are available upon reasonable request from the lead contact.

Materials

The synthesis of metal nanoparticles requires hydrogen tetrachloroaurate (II) trihydrate ($HAuCl_4 \cdot 3H_2O$, 99.99%, Alfa Aesar), trisodium citrate dihydrate, (99%, Alfa Aesar), tin(IV) chloride ($SnCl_4 \cdot 5H_2O$, 99.99%, Alfa Aesar), bismuth(III) nitrate pentahydrate ($Bi(NO_3)_3 \cdot 5H_2O$, 99.999%, Thermo Fisher Scientific), gallium(III) nitrate hydrate ($Ga(NO_3)_3 \cdot xH_2O$, 99.9%, Thermo Fisher Scientific), indium(III) chloride ($InCl_3$, 99.99%, Thermo Fisher Scientific), poly(vinylpyrrolidone) (PVP; molecular weight [MW] = 40,000, Alfa Aesar), sodium borohydride ($NaBH_4$, 97+%, Alfa Aesar), silver nitrate ($AgNO_3$, 99.9995%, Thermo Fisher Scientific), sodium bromide (NaBr, 99.99%, Alfa Aesar), and L-(+)-ascorbic acid (99%, Alfa Aesar). All chemicals were

used without further purification, and all solutions were prepared with 18.2 MΩ resistivity water. Syntheses were noted to vary slightly depending on the age of metal salt precursors, most likely because of hydration and oxidation with time.

Synthesis of Au seeds

Gold seeds were prepared in a 100-mL round-bottom flask submerged in an oil bath held at 125°C, stirred at 640 rpm. 58.56 mL of water and 1.2 mL of 10 mM $HAuCl_4$ were added to the flask and brought to reflux. At reflux, 480 μ L of 100 mM sodium citrate solution was added. The solution turned purple and then reddish pink within 3–5 min of addition of citrate. The solution was heated for 8 min, after which it was removed and allowed to cool to room temperature. The seeds were used as synthesized at ~0.7 optical density (OD).

Synthesis of Au-Sn nanoparticles

Au-Sn nanoparticles were synthesized using a seed-mediated approach.[24] 40–200 μL of $SnCl_4 \cdot 5H_2O$ (5 mM) was added to 3 mL of seeds under vigorous stirring at room temperature to achieve the desired composition. Water was then added to bring the total reaction volume to 4 mL. Approximately 0.025 mg PVP-40,000 was added directly to this mixture, and then the reaction vials were transferred to a water bath at 60°C. After remaining in the water bath for 10 min, the reaction vials were removed and stirred during addition of 120–200 μL $NaBH_4$ (260 mM). The reaction vials were returned to the water bath. The samples remained in the water bath for 20 min, after which the product was centrifuged for 8 min at 8,500 rpm, followed by removal of the supernatant and resuspension in water. For increasing Sn composition, the volume of 5 mM $SnCl_4 \cdot 5H_2O$ was varied. For example, to achieve the added Sn compositions of 24%, 30%, 37%, and 50% Sn, 38, 54, 73, and 116 μL, respectively, of $SnCl_4 \cdot 5H_2O$ (5 mM) were added. The PVP and $NaBH_4$ were adjusted as fixed ratios of 0.05:1 and 30:1, respectively, to the total molar metal (Au and Sn) content.

Synthesis of Au-Bi, Ga, In nanoparticles

The conditions and synthetic approach were similar to what was used for the Au-Sn compositions, with the following modifications. For Ga and Bi, the Au seed solutions were incubated in an ice bath for 10 min after addition of water, PVP, and the PTM solution instead of incubation in a 60°C water bath. After incubation, $NaBH_4$ was added with vigorous stirring, and the solutions were placed back in an ice bath for 10 additional minutes. For In, the Au seed solution was incubated at 60°C for 10 min after addition of water, PVP, and the PTM solution, identical to Au-Sn nanoparticle synthesis. After being removed, $NaBH_4$ was added with vigorous stirring, and the growth solutions were allowed to stand at room temperature for 10 min. All nanoparticle solutions were found to be stable for at least 1 h after synthesis.

Synthesis of Ag seeds

Aqueous solutions of sodium citrate (1 mL, 35 mM), $AgNO_3$ (250 μL, 59 mM), and NaBr (50 μL, 80 mM) were added to 1.25 mL water and stirred at room temperature for 5 min. After 4 min, 500 μL of an aqueous solution of ascorbic acid (100 mM) was added to 47.4 mL of boiling water in a 100-mL round flask that was heated with an oil bath at 125°C using a stirring rate of 600 rpm. The citrate, silver nitrate, sodium bromide solution was added to the refluxing solution after stirring for a total of 5 min (1 min after the ascorbic acid solution was added).[37] The color of the reaction changed from colorless to yellow. The solution was held at reflux for 1 h with stirring. Afterward, the solution was centrifuged at 4,100 rpm for 15 min to remove larger nanoparticles, and the supernatant was saved. The supernatant was then

centrifuged at 11,400 rpm for 30 min and resuspended in 2 mM aqueous solution of sodium citrate. The seeds were used at an OD of ~3.

Synthesis of Ag-Sn nanoparticles

Ag-Sn nanoparticles were synthesized by a seeded co-reduction method. In a typical synthesis, 1.30 mL of Ag seeds were added to 6.02 mL of water. 100 μL of 10 mM $AgNO_3$ was added under stirring, followed by addition of 160, 260, 360, and 460 μL of $SnCl_4 \cdot 5H_2O$ (5 mM). Next, 190, 220, 260, and 300 μL of sodium citrate (30 mM) was added to the reaction. The reaction vials were transferred to a water bath at 60°C for 10 min. After the 10 min elapsed, an aqueous solution of 150, 170, 190, and 215 μL $NaBH_4$ (120 mM) was added to the reaction. Similar to Au-Sn synthesis, the reaction vials were transferred to a water bath at 60°C for 20 min.

UV-visible spectroscopy

UV-visible spectra were recorded on an Agilent Technologies Cary 100 spectrophotometer.

Electron microscopy

Samples for TEM were prepared by drop-casting a dilute solution of nanoparticles onto Cu carbon type B grids (Ted Pella). TEM was performed using a Phillips CM12 operated at 120 kV. Samples for scanning electron microscopy (SEM) were prepared by centrifugation for 8 min at 8,400 rpm; afterward, the supernatant was removed, and the pellet was resuspended in water. The second centrifugation was used to obtain a pellet from which ~20 μL of solution was drop-cast onto a Si wafer. SEM and EDS was performed using a JEOL JSM 740F SEM equipped with EDAX analysis software. Elemental mapping was performed using an FEI Tecnai Osiris 200kV TEM equipped with an HAADF-STEM detector for the STEM-EDS mapping.

XRD and phase analysis

Powder XRD measurements were performed on a Rigaku Miniflex X-ray diffractometer using CuKα (λ = 1.5418 A) radiation in the 2θ range of 10°–90° and a scan rate of 1° min^{-1}. 8.0 mL of colloidal sample was concentrated to ~200 μL, drop-cast onto a zero-background Si sample holder (Rigaku), and dried at room temperature. Individual crystal phases were indexed using the crystallographic open-source database. Specific material reference numbers include Au (9013036), Au5Sn (1510571), AuSn (1510301), AuSn2 (1510306), AuSn4 (1510307), Sn (9008568), Ag (1509146), and Ag3Sn (9011118). Rietveld analysis was used to simulate the collected patterns. All samples were purified using multiple rounds of centrifugation and resuspension into water.

XPS

X-ray photo electron spectroscopy (XPS) was performed using a PHI Versaprobe II. For analysis, the spectra were corrected using a Shirley background, energies were standardized to the C1s peak, peaks were fit with Voigt functions, and the relative compositions were determined using the appropriate atomic sensitivity factors. We note that the samples exhibited limited and inconsistent amounts of adventitious carbon; this fact, coupled with the complexity of assigning oxidation states for intermetallics and complex alloys, limits their ability to be conclusively assigned. All samples were purified using multiple rounds of centrifugation and resuspension into water.

EDS-SEM compositional analysis

EDS was performed using a SEM (JEOL JSM 7401F SEM) equipped with EDAX analysis software using an accelerating voltage of 25 kV, which allows analysis of the bulk

composition of Au/Sn and Ag/Sn nanoparticles using SnL, AuM, and AgL to quantify the atomic ratios. For EDS, samples were centrifuged and drop-cast onto carbon tape. Three spots were analyzed using a maximum collection time of 100 s, and these compositions were averaged to obtain the quantities reported.

Determination of composition and extinction coefficients

Elemental analysis was used to determine the elemental composition of the digested nanoparticles. Calculation of the corresponding experimental extinction coefficients for the Au_xSn_{1-x} nanoparticles was performed by ICP-MS with a 7900 ICP-MS (Agilent Technologies, Tokyo, Japan). To prepare samples for ICP-MS analysis, 2 mL of each sample was taken for each composition studied (24%, 30%, 37%, and 50% Sn added) and centrifuged for 12 min at 10,000 rpm to isolate the nanoparticles. The supernatant was removed, and the particles were resuspended in 2 mL of water to wash away unreacted ions and surfactants The sample was again centrifuged for 12 min at 10,000 rpm. For Au_xSn_{1-x} samples, the supernatant was removed, and the nanoparticles were resuspended into solution with decreased OD ranging from 0.1–0.7 OD. 100-μL aliquots were transferred to 15-mL conical tubes, where the particles were resuspended to 1 mL by addition of 900 μL of water. The nanoparticles were then digested in 1 mL of aqua regia (3:1 HCl/HNO_3). Prior to ICP-MS analysis, the solution was diluted to a total volume of 10 mL. Triplicate measurements were made for each sample.

Extinction coefficient calculation

To determine the extinction coefficients for each nanoparticle composition, data collected with ICP-MS were converted to nanoparticles per liter concentrations before being compared with the corresponding UV-visible spectra in a Beer's law plot. The original concentration from ICP-MS before dilution is determined in two steps.

First, the weight of analyte present in the dilute solution was calculated as follows:

$$\frac{mg}{L} * prepared\ solution\ volume\ (mL) * \frac{1\ L}{1000\ mL} = mg\ of\ analyte$$

The original aliquot concentration can then be calculated as follows:

$$\frac{mg\ of\ analyte}{\frac{volume\ of\ \ sample(mL)}{1000\ mL}} = ppm\ (undiluted\ solution)$$

The number of available atoms for each of the constituent metals was calculated from the original solution concentration. Nanoparticle concentrations were then calculated using methods modified from the literature.[38,39] Briefly, the number of atoms per nanoparticle can be calculated using the following equation:

$$N = \frac{\pi}{6}\frac{\rho D^3}{M}$$

where N is the average number of atoms per nanoparticle, ρ is the density of the metal, and M is the atomic weight. To obtain the alloyed nanoparticle concentrations, the average number of atoms per nanoparticle was weighted to account for the atomic percentage of each element:

$$\frac{Total\ atoms}{((N_{Au} * atom\%) + (N_{Sn} * atom\%))} = particles$$

The nanoparticles per liter were then divided by Avogadro's number to provide molar nanoparticle concentrations for each measured sample. Beer's law plots

were then constructed in Origin, including the standard deviation in particle concentration, and a linear fit analysis was used to determine the extinction coefficient.

Generalized Mie theory

Mie theory calculations were used to calculate the optical response of alloy nanoparticles. For Au-Sn, calculations were performed assuming a linear mixing of the component's dielectric functions or using previously calculated dielectric functions for Au-Sn intermetallics. Similar calculations were performed for Au_xBi_{1-x}, Au_xGa_{1-x}, Au_xIn_{1-x}, Ag_xSn_{1-x}, Ag_xBi_{1-x}, Ag_xGa_{1-x}, and Ag_xIn_{1-x} for alloys with 5%, 10%, 15%, 20%, and 25% PTM composition. Dielectric functions were taken from the following references: Ag,[40] Au,[40] Bi,[41] Ga,[42,43] In,[44] and Sn.[45] Mie theory calculations were used to calculate the optical response of spherical metal nanoparticles with varying PTM composition, and 25 vector spherical harmonics were included for all calculations.[46,47] Extinction is reported as optical efficiency, Q, which is a unitless quantity. Surface scattering was not accounted for, and a background dielectric constant of 1.33 (water) was used for all calculations. Mie theory allows calculation of the extinction cross-section for a sphere:

$$C_{ext} = \frac{2\pi}{k^2}\sum_{n=1}^{\infty}(2n+1)\mathrm{Re}(a_n + b_n)$$

where k is the wave vector given by $k = 2\pi\varepsilon_b^{1/2}/\lambda$. a_n and b_n are the scattering coefficients, which contain the Riccati-Bessel functions used in Mie theory.[46–48] We report extinction as efficiency, which is equal to the ratio of the cross-section to the particle geometric cross-section, πa^2.

Idealized Drude-like model

The permittivity of an ideal free electron gas Drude metal was described using the Drude-Sommerfeld model:[12,33,49–51]

$$\varepsilon(\omega) = 1 - \frac{{\omega_p}^2}{\omega(\omega + i\gamma)}$$

where ω_p is the bulk plasma frequency and γ is a phenomenological scattering rate. For the metals described here, the scattering rate was set to 0.01 unless noted otherwise. The dielectric function was used for calculating the extinction efficiency using Mie theory.

SUPPLEMENTAL INFORMATION

Supplemental information can be found online at https://doi.org/10.1016/j.matt.2023.01.004.

ACKNOWLEDGMENTS

We are grateful to Prof. Vicki Keast, University of Newcastle, for sharing calculated dielectric functions for the Au-Sn intermetallic compounds. This work relates to Department of Navy awards N00014-20-1-2858 and N00014-22-1-2654 issued by the Office of Naval Research. Characterization was supported in part by the National Science Foundation Major Research Instrumentation program under grant 2216240. This work was also partially supported by the University of Massachusetts Lowell and the Commonwealth of Massachusetts. We are grateful to the UMass Lowell Core Research Facilities and the MIT Material Research Laboratory for use of the PHI Versaprobe II and to the Yale YINQE facility for use of the FEI Tecnai Osiris. M.E.K. gratefully acknowledges support from the American Association of University Women American Postdoctoral Fellowship. M.V.F.G. gratefully acknowledges

support from the RIST Institute for the Sustainability and Energy Fellowship. N.L.M. gratefully acknowledges support through the Kennedy Colleges of Science KCS Science Scholars program and the ACS NESACS Chapter Norris-Richards Fellowship.

AUTHOR CONTRIBUTIONS

M.V.F.G. and M.B.R. designed the systems, collected and analyzed data, validated the methods and analysis, and wrote the manuscript. M.E.K. and N.L.M. collected and analyzed data, validated the methods and analysis, and wrote the manuscript. C.S.S. and S.J. collected and analyzed data and wrote the manuscript.

DECLARATION OF INTERESTS

The authors declare no competing interests.

Received: May 5, 2022
Revised: December 7, 2022
Accepted: January 5, 2023
Published: February 2, 2023

REFERENCES

1. Brongersma, M.L., Halas, N.J., and Nordlander, P. (2015). Plasmon-induced hot carrier science and technology. Nat. Nanotechnol. *10*, 25–34. https://doi.org/10.1038/nnano.2014.311.

2. Kelly, K.L., Coronado, E., Zhao, L.L., and Schatz, G.C. (2003). The optical properties of metal nanoparticles: the influence of size, shape, and dielectric environment. J. Phys. Chem. B *107*, 668–677. https://doi.org/10.1021/jp026731y.

3. Linic, S., Chavez, S., and Elias, R. (2021). Flow and extraction of energy and charge carriers in hybrid plasmonic nanostructures. Nat. Mater. *20*, 916–924. https://doi.org/10.1038/s41563-020-00858-4.

4. Prodan, E., Radloff, C., Halas, N.J., and Nordlander, P. (2003). A hybridization model for the plasmon response of complex nanostructures. Science *302*, 419–422. https://doi.org/10.1126/science.1089171.

5. Naldoni, A., Shalaev, V.M., and Brongersma, M.L. (2017). Applying plasmonics to a sustainable future. Science *356*, 908–909. https://doi.org/10.1126/science.aan5802.

6. Cortie, M.B., and McDonagh, A.M. (2011). Synthesis and optical properties of hybrid and alloy plasmonic nanoparticles. Chem. Rev. *111*, 3713–3735. https://doi.org/10.1021/cr1002529.

7. Zhou, M., Li, C., and Fang, J. (2021). Noble-metal based random alloy and intermetallic nanocrystals: syntheses and applications. Chem. Rev. *121*, 736–795. https://doi.org/10.1021/acs.chemrev.0c00436.

8. Mubeen, S., Lee, J., Singh, N., Krämer, S., Stucky, G.D., and Moskovits, M. (2013). An autonomous photosynthetic device in which all charge carriers derive from surface plasmons. Nat. Nanotechnol. *8*, 247–251. https://doi.org/10.1038/nnano.2013.18.

9. Alexander, D.T.L., Forrer, D., Rossi, E., Lidorikis, E., Agnoli, S., Bernasconi, G.D., Butet, J., Martin, O.J.F., and Amendola, V. (2019). Electronic structure-dependent surface plasmon resonance in single Au–Fe nanoalloys. Nano Lett. *19*, 5754–5761. https://doi.org/10.1021/acs.nanolett.9b02396.

10. Cargnello, M., Agarwal, R., Klein, D.R., Diroll, B.T., Agarwal, R., and Murray, C.B. (2015). Uniform bimetallic nanocrystals by high-temperature seed-mediated colloidal synthesis and their catalytic properties for semiconducting nanowire growth. Chem. Mater. *27*, 5833–5838. https://doi.org/10.1021/acs.chemmater.5b02900.

11. Link, S., Wang, Z.L., and El-Sayed, M.A. (1999). Alloy formation of gold−silver nanoparticles and the dependence of the plasmon absorption on their composition. J. Phys. Chem. B *103*, 3529–3533. https://doi.org/10.1021/jp990387w.

12. Blaber, M.G., Arnold, M.D., and Ford, M.J. (2010). A review of the optical properties of alloys and intermetallics for plasmonics. J. Phys. Condens. Matter *22*, 143201. https://doi.org/10.1088/0953-8984/22/14/143201.

13. Naik, G.V., Shalaev, V.M., and Boltasseva, A. (2013). Alternative plasmonic materials: beyond gold and silver. Adv. Mater. *25*, 3264–3294. https://doi.org/10.1002/adma.201205076.

14. Cortie, M.B., Arnold, M.D., and Keast, V.J. (2020). The quest for zero loss: unconventional materials for plasmonics. Adv. Mater. *32*, e1904532. https://doi.org/10.1002/adma.201904532.

15. Singh, R., and Soni, R.K. (2014). Plasmonics properties of trimetallic Al@Al2O3@Ag@Au and Al@Al2O3@AuAg nanostructures. Appl. Phys. A *116*, 955–967. https://doi.org/10.1007/s00339-014-8455-7.

16. Fonseca Guzman, M.V., and Ross, M.B. (2021). Radiative contributions dominate plasmon broadening for post-transition metals in the ultraviolet. J. Phys. Chem. C *125*, 19428–19437. https://doi.org/10.1021/acs.jpcc.1c03895.

17. King, M.E., Fonseca Guzman, M.V., and Ross, M.B. (2022). Material strategies for function enhancement in plasmonic architectures. Nanoscale *14*, 602–611. https://doi.org/10.1039/d1nr06049j.

18. Knight, M.W., King, N.S., Liu, L., Everitt, H.O., Nordlander, P., and Halas, N.J. (2014). Aluminum for plasmonics. ACS Nano *8*, 834–840. https://doi.org/10.1021/nn405495q.

19. Melen, R.L. (2019). Frontiers in molecular p-block chemistry: from structure to reactivity. Science *363*, 479–484. https://doi.org/10.1126/science.aau5105.

20. Leitao, E.M., Jurca, T., and Manners, I. (2013). Catalysis in service of main group chemistry offers a versatile approach to p-block molecules and materials. Nat. Chem. *5*, 817–829. https://doi.org/10.1038/nchem.1749.

21. Lee, K.-S., and El-Sayed, M.A. (2006). Gold and silver nanoparticles in sensing and imaging: sensitivity of plasmon response to size, shape, and metal composition. J. Phys. Chem. B *110*, 19220–19225. https://doi.org/10.1021/jp062536y.

22. Keast, V.J., Barnett, R.L., and Cortie, M.B. (2014). First principles calculations of the optical and plasmonic response of Au alloys and intermetallic compounds. J. Phys. Condens. Matter *26*, 305501. https://doi.org/10.1088/0953-8984/26/30/305501.

23. Massalski, T.B., and Okamoto, H.; ASM International (1990). Binary Alloy Phase Diagrams, 2nd Edition (ASM International).

24. Ismail, A.M., Samu, G.F., Balog, Á., Csapó, E., and Janáky, C. (2018). Composition-dependent electrocatalytic behavior of Au–Sn bimetallic nanoparticles in carbon dioxide reduction. ACS Energy Lett. *4*, 48–53. https://doi.org/10.1021/acsenergylett.8b01996.

25. Yu, K., Yao, T., Pan, Z., Wei, S., and Xie, Y. (2009). Structural evolution in the nanoscale diffusion process: a Au–Sn bimetallic system. Dalton Trans. 10353–10358. https://doi.org/10.1039/b916215a.

26. Yasuda, H., and Furuya, K. (2000). Spontaneous alloying of tin atoms into nanometer-sized gold clusters and phase stability in the resultant alloy clusters. Eur. Phys. J. D *10*, 279. https://doi.org/10.1007/s100530050549.

27. Arora, N., and Jagirdar, B.R. (2014). From (Au5Sn + AuSn) physical mixture to phase pure AuSn and Au5Sn intermetallic nanocrystals with tailored morphology: digestive ripening assisted approach. Phys. Chem. Chem. Phys. *16*, 11381–11389. https://doi.org/10.1039/c4cp00249k.

28. Tan, Q., Deng, C., Mao, Y., and He, G. (2011). Evolution of primary phases and high-temperature compressive behaviors of as-cast AuSn20 alloys prepared by different solidification pathways. Gold Bull. *44*, 27–35. https://doi.org/10.1007/s13404-011-0004-y.

29. Leonard, B.M., and Schaak, R.E. (2006). Multistep solution-mediated formation of AuCuSn2: mechanistic insights for the guided design of intermetallic solid-state materials and complex multimetal nanocrystals. J. Am. Chem. Soc. *128*, 11475–11482. https://doi.org/10.1021/ja062475h.

30. Osugi, S., Takano, S., Masuda, S., Harano, K., and Tsukuda, T. (2021). Few-nm-sized, phase-pure Au5Sn intermetallic nanoparticles: synthesis and characterization. Dalton Trans. *50*, 5177–5183. https://doi.org/10.1039/d1dt00132a.

31. Kim, Y., Johnson, R.C., Li, J., Hupp, J.T., and Schatz, G.C. (2002). Synthesis, linear extinction, and preliminary resonant hyper-Rayleigh scattering studies of gold-core/silver-shell nanoparticles: comparisons of theory and experiment. Chem. Phys. Lett. *352*, 421–428. https://doi.org/10.1016/s0009-2614(01)01506-8.

32. Gordon, T.R., and Schaak, R.E. (2014). Synthesis of hybrid Au-In2O3 nanoparticles exhibiting dual plasmonic resonance. Chem. Mater. *26*, 5900–5904. https://doi.org/10.1021/cm502396d.

33. Pellarin, M., Broyer, M., Lermé, J., Lebeault, M.-A., Ramade, J., and Cottancin, E. (2016). Plasmon resonances tailored by Fano profiles in silver-based core–shell nanoparticles. Phys. Chem. Chem. Phys. *18*, 4121–4133. https://doi.org/10.1039/c5cp07113e.

34. Ross, M.B., De Luna, P., Li, Y., Dinh, C.-T., Kim, D., Yang, P., and Sargent, E.H. (2019). Designing materials for electrochemical carbon dioxide recycling. Nat. Catal. *2*, 648–658. https://doi.org/10.1038/s41929-019-0306-7.

35. Cable, R.E., and Schaak, R.E. (2006). Reacting the unreactive: a toolbox of low-temperature solution-mediated reactions for the facile interconversion of nanocrystalline intermetallic compounds. J. Am. Chem. Soc. *128*, 9588–9589. https://doi.org/10.1021/ja0627996.

36. Gamler, J.T.L., Ashberry, H.M., Skrabalak, S.E., and Koczkur, K.M. (2018). Random alloyed versus intermetallic nanoparticles: a comparison of electrocatalytic performance. Adv. Mater. *30*, e1801563. https://doi.org/10.1002/adma.201801563.

37. Li, H., Xia, H., Ding, W., Li, Y., Shi, Q., Wang, D., and Tao, X. (2014). Synthesis of monodisperse, Quasi-spherical silver nanoparticles with sizes defined by the nature of silver precursors. Langmuir *30*, 2498–2504. https://doi.org/10.1021/la4047148.

38. Liu, X., Atwater, M., Wang, J., and Huo, Q. (2007). Extinction coefficient of gold nanoparticles with different sizes and different capping ligands. Colloids Surf. B Biointerfaces *58*, 3–7. https://doi.org/10.1016/j.colsurfb.2006.08.005.

39. O'Brien, M.N., Jones, M.R., Brown, K.A., and Mirkin, C.A. (2014). Universal noble metal nanoparticle seeds realized through iterative reductive growth and oxidative dissolution reactions. J. Am. Chem. Soc. *136*, 7603–7606. https://doi.org/10.1021/ja503509k.

40. Johnson, P.B., and Christy, R.W. (1972). Optical constants of the noble metals. Phys. Rev. B *6*, 4370–4379. https://doi.org/10.1103/PhysRevB.6.4370.

41. de Sande, J.C.G., Missana, T., and Afonso, C.N. (1996). Optical properties of pulsed laser deposited bismuth films. J. Appl. Phys. *80*, 7023–7027. https://doi.org/10.1063/1.363775.

42. Hunderi, O., and Ryberg, R. (1974). Band structure and optical properties of gallium. J. Phys. F: Met. Phys. *4*, 2084–2095. https://doi.org/10.1088/0305-4608/4/11/032.

43. Jezequel, G., Lemonnier, J.C., and Thomas, J. (1977). Optical properties of gallium films between 2 and 15 eV. J. Phys. F Met. Phys. *7*, 1613–1622. https://doi.org/10.1088/0305-4608/7/8/028.

44. Koyama, R.Y., Smith, N.V., and Spicer, W.E. (1973). Optical properties of indium. Phys. Rev. B *8*, 2426–2432. https://doi.org/10.1103/PhysRevB.8.2426.

45. MacRae, R.A., Arakawa, E.T., and Williams, M.W. (1967). Optical properties of vacuum-evaporated white tin. Phys. Rev. *162*, 615–620. https://doi.org/10.1103/PhysRev.162.615.

46. Bohren, C.F., and Huffman, D.R. (1983). Absorption and Scattering of Light by Small Particles (Wiley).

47. Mie, G. (1908). Beiträge zur Optik trüber Medien, speziell kolloidaler Metallösungen. Ann. Phys. *330*, 377–445. https://doi.org/10.1002/andp.19083300302.

48. Fan, X., Zheng, W., and Singh, D.J. (2014). Light scattering and surface plasmons on small spherical particles. Light Sci. Appl. *3*, e179. https://doi.org/10.1038/lsa.2014.60.

49. Kreibig, U., and Vollmer, M. (1995). Optical Properties of Metal Clusters (Springer). https://doi.org/10.1007/978-3-662-09109-8.

50. Wang, F., and Shen, Y.R. (2006). General properties of local plasmons in metal nanostructures. Phys. Rev. Lett. *97*, 206806. https://doi.org/10.1103/PhysRevLett.97.206806.

51. Ashcroft, N.W., and Mermin, N.D. (1976). Solid State Physics (Saunders College Publishing).